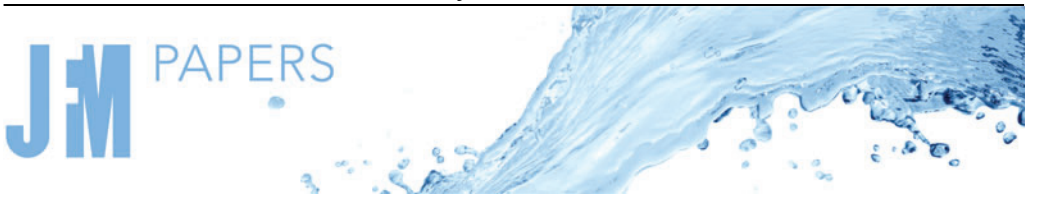
J. Fluid Mech. (2024), *vol*. 993, A12, doi:10.1017/jfm.2024.634



Net spanwise flow induced by symmetry-breaking streamwise homogeneous surfaces

Oleksandr Zhdanov[1],† **and Angela Busse**[1]

[1]James Watt School of Engineering, University of Glasgow, Glasgow G12 8QQ, UK

(Received 7 June 2024; revised 19 July 2024; accepted 20 July 2024)

The influence of symmetry-breaking effects of ridge-type roughness on secondary currents in turbulent channel flow is investigated using direct numerical simulations. The ridges have triangular cross-section, which is systematically varied from isosceles to right-angled triangle, introducing an imbalance to the slopes of the ridges' lateral surfaces while the streamwise homogeneity of the surfaces is maintained. In all cases, secondary current vortices are produced, but asymmetric ridge cross-sections break the symmetry of these vortices. As a result of the asymmetry-induced misalignment and imbalance in the secondary current vortices, net spanwise flow emerges. The magnitude of the spanwise flow increases with the slope ratio of the ridge lateral surfaces and significantly modifies the mean flow topology, leading to the merging of critical points in the case of the right-angled triangular ridge shape. Within the cavities, the net spanwise flow is accompanied by a non-zero mean spanwise pressure gradient, while from the perspective of the outer flow, the scalene ridge surfaces have a similar effect as a wall that is slowly moving in the spanwise direction. Overall, the present results suggest the existence of a special type of Prandtl's secondary currents of the second kind, namely those that result in net spanwise flow.

Key words: boundary layer structure, turbulent boundary layers, turbulence simulation

1. Introduction

Secondary currents encompass flows that emerge in the cross-stream plane normal to the primary flow direction. Their presence in turbulent flows can result in two different flow patterns in the cross-stream plane: identifiable streamwise vortices and spanwise/cross-flow (Bradshaw 1987). The former represent secondary currents of the Prandtl's second kind (Prandtl 1952), which originate from turbulence anisotropy and

† Email address for correspondence: oleksandr.zhdanov@glasgow.ac.uk

© The Author(s), 2024. Published by Cambridge University Press. This is an Open Access article, distributed under the terms of the Creative Commons Attribution licence (http://creativecommons.org/licenses/by/4.0), which permits unrestricted re-use, distribution and reproduction, provided the original article is properly cited.

https://doi.org/10.1017/jfm.2024.634 Published online by Cambridge University Press

spatial gradients of the Reynolds stresses, while the latter is attributed to the presence of a spanwise pressure gradient. In the context of roughness, secondary currents are known to emerge over spanwise inhomogeneous rough surfaces (Hinze 1967), where they are represented by a streamwise aligned pair of vortices separated by high- and low-momentum pathways, i.e. downwash and upwash flow regions. Although secondary current vortices (SCVs) are weak compared with the mean flow, they can introduce significant spanwise heterogeneities to the mean flow field, giving rise to elevated levels of dispersive stresses, which can propagate up to the outer edge of the boundary layer. Therefore, SCVs affect the mean flow and turbulence statistics, as well as influence exchange of momentum and mixing.

Over the last decade, secondary currents over rough surfaces have received significant attention from the fluid mechanics community. Two main classes of rough surfaces have been investigated experimentally and numerically in this context: ridge-type roughness, i.e. surfaces with spanwise variation in topography, and strip-type roughness, which represents surfaces with spanwise variation in skin friction (Wang & Cheng 2006). For both classes of surfaces, secondary currents were found in the form of SCVs, whose extent primarily depends on the size and spacing of the spanwise surface features. For ridge-type roughness, spanwise spacing between adjacent ridges was identified as a key parameter that governs the size and strength of SCVs (Vanderwel & Ganapathisubramani 2015; Hwang & Lee 2018; Zampiron, Cameron & Nikora 2020). When spacing reaches the outer length scale of the flow, SCVs become space filling and their strength is maximised (Vanderwel & Ganapathisubramani 2015). Other parameters, such as ridge width and shape also have been found to influence the SCVs' strength (Hwang & Lee 2018; Medjnoun, Vanderwel & Ganapathisubramani 2020; Zhdanov, Jelly & Busse 2024). However, in all cases reported in the literature the secondary currents materialised in the form of identifiable streamwise vortices, while no presence of net spanwise flow has been reported to date for either ridge-type or strip-type roughness. In the present study, we consider a special class of ridge-type roughness, namely symmetry-breaking streamwise homogeneous surfaces composed of ridges with asymmetric cross-section, which induce not only SCVs but also produce net spanwise flow.

Despite the abundance of literature on secondary currents generated by ridge-type rough surfaces, all previous studies share the same feature, namely the considered ridges have a wall-normal axis of symmetry with respect to the surface on which they are placed. As a result, the secondary current vortices formed in between and/or above ridges are symmetric, i.e. statistically the same differing only in their rotational direction. Compared with other commonly studied cross-sectional geometries, such as rectangular or semicircular ridges, triangular ridges allow for a wider range of modifications to their cross-section. In addition to equilateral and isosceles, triangular ridges can have scalene cross-section with different slopes of their lateral surfaces and therefore break the symmetry of the ridge with respect to the wall-normal direction. For isosceles triangular ridges, we have previously established that narrow ridges, i.e. ridges with higher lateral slopes, produce stronger SCVs compared with wide ridges, i.e. ridges with lower lateral slopes (Zhdanov *et al.* 2024). Since isosceles ridges preserve the symmetry with respect to the wall-normal direction, the vortices in the SCV pair that forms over each ridge are of equal strength and size. As will be shown in the following, scalene ridge cross-sections introduce symmetry-breaking effects due to the imbalance in lateral ridge slopes, significantly alter the SCV topology and induce a net spanwise flow.

The aim of the present study is to systematically investigate the influence of asymmetric ridge cross-section on secondary currents and other effects induced by breaking the left–right symmetry of a ridged surface. To this end, direct numerical simulations of

https://doi.org/10.1017/jfm.2024.634 Published online by Cambridge University Press

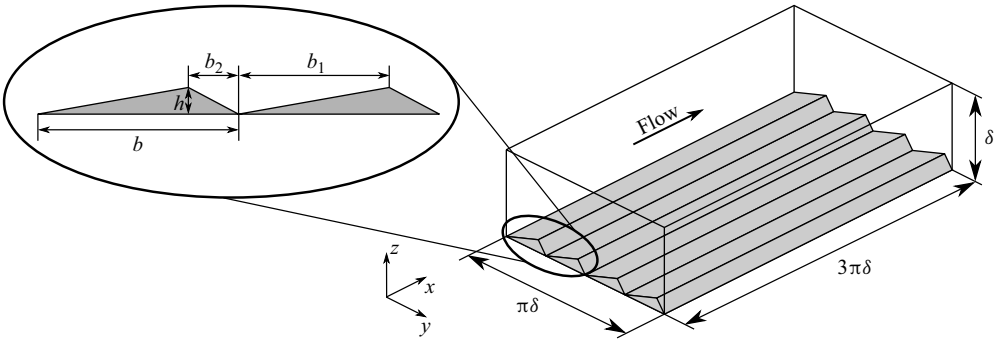


Figure 1. Schematic of a channel with ridge-type roughness used for DNS (not to scale). Here, δ is the channel half-height, h is the ridge height, b is the ridge base width and b_1 and b_2 are the left and right ridge base segments. The channel is symmetric with respect to the centreplane and only its lower half is shown.

turbulent channel flow are conducted over ridged surfaces with systematically varied degree of cross-sectional asymmetry. In § 2 the numerical methodology is outlined, results are presented and discussed in § 3 and conclusions follow in § 4.

2. Numerical methodology

Direct numerical simulations (DNS) of incompressible fully developed turbulent channel flow over ridge-type rough surfaces are performed using the code iIMB (Busse, Lützner & Sandham 2015). The code has been validated and used in previous studies on surfaces composed of regular roughness elements (e.g. Busse & Zhdanov 2022), including ridge-type roughness that generates secondary currents (Zhdanov *et al.* 2024). The velocity components in the streamwise (x), spanwise (y) and wall-normal (z) directions are u, v and w, respectively. The flow is driven by a constant (negative) mean streamwise pressure gradient Π, which determines the mean friction velocity in the simulation as $u_\tau = \sqrt{-\Pi\delta/\rho}$, where ρ is the constant density and δ is the channel half-height.

A schematic of a channel with ridge-type roughness used for the present DNS is presented in figure 1. The domain has size ($L_x \times L_y \times L_z$) of $3\pi\delta \times \pi\delta \times 2\delta$ and is discretised with $1152 \times 576 \times 512$ computational grid points. Spatial resolution is uniform in the streamwise and spanwise directions with $\Delta x^+ = 4.5$ and $\Delta y^+ = 3$. In the wall-normal direction, constant grid spacing is applied up to the ridge crest with $\Delta z^+_{min} = 0.67$ and is gradually increased above, reaching a maximum value of $\Delta z^+_{max} = 4.69$ at the channel centreplane. The ridges cover both the lower and the upper channel walls which are mirrored with respect to the channel centreplane. The ridge geometry is resolved using an iterative version of the embedded boundary method by Yang & Balaras (2006). Periodic boundary conditions are prescribed in the streamwise and spanwise directions, while ridge surfaces are treated as no-slip walls.

Four surfaces fully covered with ridges of triangular cross-section are considered. In all cases, ridges have fixed height, $h/\delta = 0.08$, and base width, $b/\delta = \pi/4$ (see inset in figure 1). Since the entire channel wall is covered with ridges, the spacing is equivalent to the ridge base width. The ridges with the chosen width/spacing are expected to generate significant secondary currents (Zhdanov *et al.* 2024). The triangular ridge cross-section is systematically varied between cases by changing the ratio of ridge base segments (b_1/b_2),

https://doi.org/10.1017/jfm.2024.634 Published online by Cambridge University Press

which are obtained by drawing a height to the ridge base. This corresponds to the variation of the ratio between the lateral slopes of the ridge. Starting from an isosceles triangular cross-section ($b_1/b_2 = 1$), the symmetry of the cross-section is broken by increasing the ratio of ridge base segments first to 3, then to 7 and finally to ∞, which corresponds to the right-angled triangle. Throughout the paper the cases are denoted by using their corresponding ratio b_1/b_2 denoted by R followed by the value of R. For instance, the case with ridge base segments ratio of 7 is denoted as R7. Since all cases are streamwise homogeneous, the streamwise effective slope ES_x (Napoli, Armenio & De Marchis 2008) is zero in all cases. The spanwise effective slope ES_y (Jelly *et al.* 2022) is equal to $ES_y = 2h/b \approx 0.2037$ for all surfaces, since the ridge height, base width and spacing are constant across all studied cases.

All simulations are conducted at a constant friction Reynolds number of 550, which is defined here as $Re_\tau \equiv u_\tau \delta/\nu$, where ν is the kinematic viscosity. In each simulation, flow statistics are acquired for $Tu_\tau/\delta = 100$ non-dimensional time units after the initial transient, which corresponds to a minimum of 176 flow through times. Statistical quantities are computed using a double-averaged (time-then-space) methodology (Raupach & Shaw 1982; Nikora *et al.* 2007) together with intrinsic averaging (Gray & Lee 1977), i.e. only the fluid occupied region is considered when computing averages below the ridge crests. In addition, for each simulation 2500 instantaneous three-dimensional snapshots were collected. The snapshots are separated by 22 viscous-scaled time units, $\Delta t^+ \equiv \Delta t u_\tau^2/\nu = 22$. The reference smooth-wall DNS is conducted at matched flow conditions, domain size and grid resolution. Throughout the paper, superscript $+$ indicates viscous-scaled quantities, e.g. $v^+ = v/u_\tau$, $\bar{\cdot}$ denotes time-averaged quantities and $\langle\cdot\rangle$ denotes intrinsic averaging over wall-parallel (x–y) planes.

3. Results

3.1. *Mean flow and global properties*

The mean streamwise velocity fields for all four ridged surfaces (R1 to R∞) are presented in figure 2 with superimposed in-plane velocity vectors. As expected from previous studies on turbulent flow over streamwise aligned ridges with symmetric triangular cross-sections (e.g. Stroh *et al.* 2020; Zampiron *et al.* 2020; Zhdanov *et al.* 2024), the present triangular ridges produce SCVs with upwash regions above the ridge crests and downwash over the cavity formed by the lateral surfaces of adjacent ridges accompanied by spanwise heterogeneity of the mean flow field. Isosceles ridges with equal slope of their lateral surfaces (case R1) produce symmetric SCVs with the downwash region aligned with the bottom of the valley between ridges (figure 2*a*). As the ridge cross-section becomes scalene, the asymmetry in geometry is reflected in the induced secondary current vortices: the vortex formed on the high-slope ridge side is more pronounced compared with its counterpart formed on the low-slope side, and this trend continues as R increases (figure 2*b–d*). Thus, as expected, an asymmetric ridge cross-section leads to an imbalance in vortices formed over each side of the ridge. The high-slope side vortex suppresses the vortex over the low-slope side and occupies part of the flow above the low-slope side of the ridge. As a result, downwash is not aligned with the bottom of the valley, as in case R1, but occurs over the ridge surface with lower slope.

As is evident from the in-plane velocity vectors, especially in the outer layer, there is a net spanwise flow in the channel for the scalene ridge cases, i.e. scalene ridges produce cross-flow. The net spanwise flow is quantified in figure 3(*a*), where $\langle\bar{v}\rangle^+$ profiles are plotted for all ridge-type cases together with reference smooth-wall data. Before discussing

https://doi.org/10.1017/jfm.2024.634 Published online by Cambridge University Press

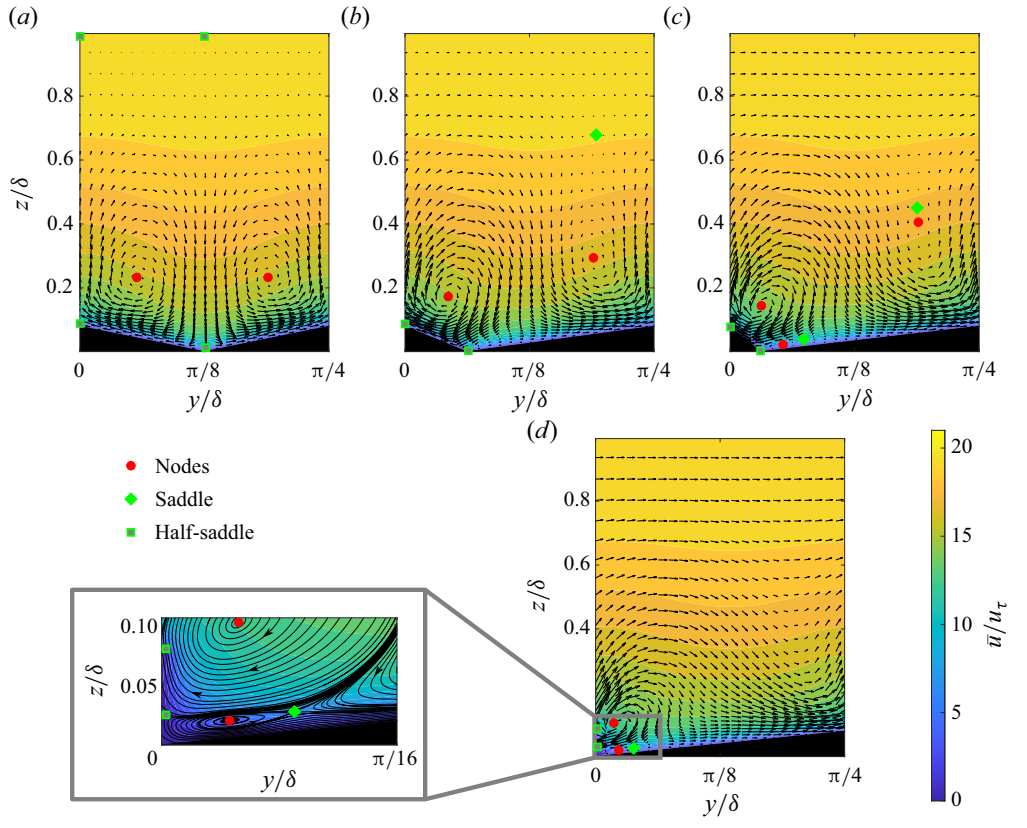


Figure 2. Contours of the phase-averaged mean streamwise velocity with superimposed in-plane velocity vectors (downsampled for clarity): (*a*) R1, (*b*) R3, (*c*) R7, (*d*) R∞. Locations of critical points in the flow are marked in each panel. For critical points located at the spanwise boundaries only one point is shown.

the present results, it should be noted that, for smooth-wall conditions, the mean spanwise velocity is expected to be zero provided that the flow statistics are perfectly converged. However, since in DNS flow statistics are averaged over finite time and domain size, for the present smooth-wall case $\langle\bar{v}\rangle^+$ is not strictly zero but exhibits small deviations. This is a typical result, as can be seen from the DNS data by Lee & Moser (2015) for smooth-wall channel flow, which are also plotted in figure 3(*a*), obtained at the same Re_τ in a much bigger channel ($L_x \times L_y = 8\pi\delta \times 3\pi\delta$) but for a shorter time-averaging period. For case R1 (isosceles ridges), $\langle\bar{v}\rangle^+$ remains close to zero, but, once the ridge cross-section becomes scalene, finite values of spanwise velocity are observed across the channel half-height. In the scalene ridge cases (R3, R7 and R∞) the magnitude of the double-averaged spanwise velocity is higher by a couple of orders of magnitude compared with R1 and the smooth-wall cases. An additional DNS was conducted to verify that scalene ridges generate net spanwise flow using the same set-up as described in § 2. For this simulation, denoted as R7f, the ridged-wall geometry is the same as for case R7 but the ridges are flipped horizontally. As is evident from figure 3(*a*), case R7f produces net spanwise flow in the opposite direction compared with case R7, while the $\langle\bar{v}\rangle^+$ magnitude closely matches for both cases. Therefore, the observed net spanwise flow over the scalene ridges is a physical effect and not an artefact of finite averaging.

https://doi.org/10.1017/jfm.2024.634 Published online by Cambridge University Press

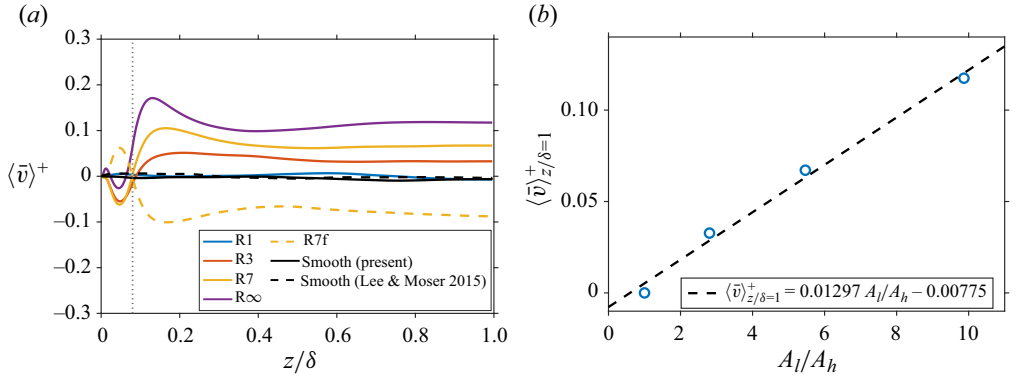


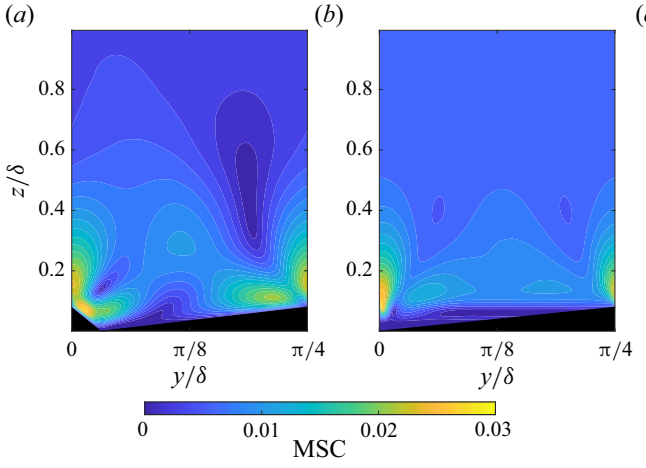
Figure 3. (*a*) Double-averaged profiles of spanwise velocity, (*b*) spanwise velocity at the channel centreplane as a function of the ratio of the wetted areas of the ridge sides.

The spanwise flow direction is not constant across z/δ: above the ridge crest $\langle\bar{v}\rangle^+$ has mostly positive values, i.e. the flow direction is away from the high-slope side of the ridge, while below the mean spanwise velocity is largely negative, i.e. the spanwise flow is directed towards the ridge side with high slope. In addition, for cases R7 and R∞ there is a small region at the bottom of the cavity between the ridge sides, which is more pronounced in the latter case, where the spanwise flow direction matches the direction above the crests. This region corresponds to an additional vortex formed under the main SCV in these cases as will be discussed in § 3.2.

Below the ridge crest an increase in R from 3 to 7 has only a minor effect on the spanwise velocity, while further increase to ∞ leads to a drop in $\langle\bar{v}\rangle^+$ values. Above the ridge crests, the spanwise flow becomes stronger as the ratio between ridge slopes increases with the highest $\langle\bar{v}\rangle^+$ observed for the case R∞. A peak emerges in the $\langle\bar{v}\rangle^+$ profiles for the asymmetric ridge cases, which is more pronounced in the R7 and R∞ cases. This peak is located just above the nodal point over the high-slope ridge side (discussed in § 3.2) and corresponds to the lower boundary of the upper sidewash region of the SCV above this ridge side. With respect to the low-slope ridge side the peak location falls within the lower sidewash region of the corresponding secondary current structure (figure 2). Above ridge crest for $z/\delta \gtrapprox 0.5$, the net spanwise velocity approaches a nearly constant value in the outer layer. The spanwise velocity magnitude exhibits an approximately linear correlation with the ratio of the wetted areas of the ridge sides, A_l/A_h, where A_l is the wetted area of the low-slope side and A_h is the wetted area of the high-slope side (figure 3*b*). Although the magnitude of net spanwise flow is low relative to the mean streamwise flow, it is comparable to the vertical velocity in the upwash and downwash regions and spanwise velocity in the sidewash regions of the SCVs. The latter is particularly evident from figures 2(*c*)–2(*d*), where the top sidewash region of the SCV generated over the low-slope ridge side is completely suppressed by the spanwise flow, and the mean spanwise flow direction in this region is reversed compared with the case R1, where no spanwise flow is present (figure 2*a*).

Despite the presence of SCVs and, in the case of asymmetric ridges, net spanwise flow, the studied surfaces exhibit a good level of outer layer similarity, as is evident from the collapse of the streamwise velocity profiles with the smooth-wall data when plotted in defect form (figure 5*a*). It should be noted that, in our previous study (Zhdanov *et al.* 2024), ridged surfaces with equilateral triangular cross-section with the same spanwise spacing

https://doi.org/10.1017/jfm.2024.634 Published online by Cambridge University Press



(c)

$\tilde{v} = \bar{v} - \langle \bar{v} \rangle(z)$

Case	$\left(\frac{\sqrt{\bar{v}^2+\bar{w}^2}}{U_b}\right)_{max}$	$\left(\frac{\sqrt{\tilde{v}^2+\bar{w}^2}}{U_b}\right)_{max}$
R1	0.0161	0.0161
R3	0.0246	0.0197
R7	0.0280	0.0243
R∞	0.0291	0.0290
R7f	0.0280	0.0240

Figure 4. Contours of the phase-averaged magnitude of the secondary currents (MSC) for case R7 (*a*) with and (*b*) without net spanwise flow, (*c*) maximum magnitude of the secondary currents for all studied cases.

also exhibited a good collapse. The strength of secondary currents is often characterised based on the maximum magnitude of the induced secondary motions compared with the bulk flow velocity $(\sqrt{\bar{v}^2 + \bar{w}^2}/U_b)_{max}$ (see, e.g. Stroh *et al.* 2020). A representative example of the magnitude of secondary currents is shown in figure 4(*a*) for case R7. The strength of secondary currents for each case is shown in figure 4(*c*). The symmetric ridge case (R1) produces the weakest secondary currents and their maximum magnitude of 1.61 % of U_b is lower compared with 4.4 % found by Medjnoun *et al.* (2020) and Zhdanov *et al.* (2024) and 6.6 % reported by Stroh *et al.* (2020). This result is expected, since the ridges in the present study are wider compared with those investigated in the referenced studies and with an increase of ridge base width the strength of secondary currents is known to decrease (see e.g. Hwang & Lee 2018; Zhdanov *et al.* 2024). In addition, in contrast to previous studies, where the location of maximum magnitude of secondary currents is associated with the upwash regions over ridge crests, for case R1 it is located over the ridge sides. This can be attributed to the full coverage of the channel walls with ridges, while in the referenced studies the ridges were separated by smooth-wall sections, i.e. the ridge base width was smaller than the ridge spacing. An increase in the ridge cross-sectional asymmetry results in progressively higher $(\sqrt{\bar{v}^2 + \bar{w}^2}/U_b)_{max}$, reaching the highest value for R∞, which exceeds the R1 case by a factor of 1.8. For the asymmetric cases R3 and R7, the maximum magnitude of secondary currents is found over the high-slope ridge side (see figure 4(*a*) for R7), while for R∞, where the high-slope side is a vertical wall, it is located in the upwash region above the ridge crest.

It should be noted that the magnitude of secondary currents grows with the increase in the net spanwise flow, since $\bar{v}$ is included in its definition. By subtracting the double-averaged spanwise velocity profile from the time-averaged spanwise velocity field it is possible to eliminate the direct contributions of the net spanwise flow (see figure 4*b*) to the secondary current strength. For cases R3, R7 and R7f subtracting the net spanwise flow for a given wall-normal location results in a reduction of the maximum magnitude of secondary currents (figure 4*c*) and shifts its location to the region above ridge crest (see figure 4(*b*) for R7). In contrast, for R∞ no significant change in the maximum secondary current strength is observed, since it is associated with high $\bar{w}$ values in the upwash region.

https://doi.org/10.1017/jfm.2024.634 Published online by Cambridge University Press

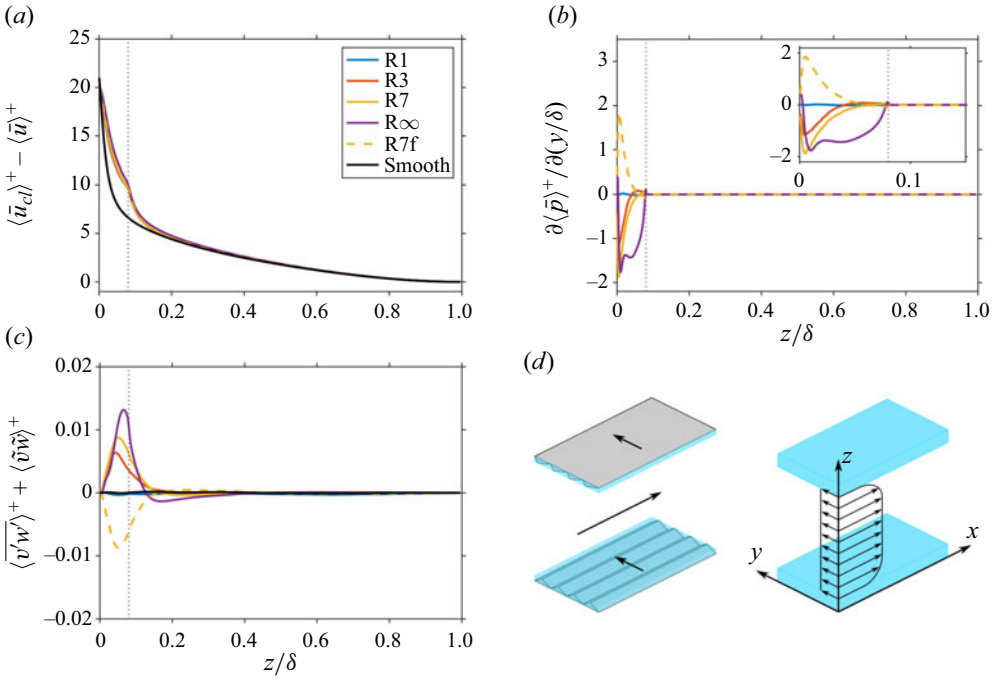


Figure 5. Double-averaged profiles of (*a*) streamwise velocity profiles in defect form, (*b*) spanwise pressure gradient, (*c*) sum of in-plane Reynolds and dispersive shear stress $\langle \overline{v'w'} \rangle^+ + \langle \tilde{v}\tilde{w} \rangle^+$. Reference smooth-wall data are also presented for panels (*a*,*c*). The thin vertical dotted line marks location of the ridge crest. (*d*) Schematic of the spanwise flow induced by surfaces with scalene ridges.

3.2. *Flow topology*

The presence of net spanwise flow due to the asymmetric ridge cross-section influences the flow topology, which in the following is analysed through critical points (Hunt *et al.* 1978). For each case nodes (N), saddles (S), half-nodes (N') and half-saddles (S') are identified and marked in figure 2. For a singly connected domain, as is the case for the present DNS, the total number of critical points must satisfy the identity (Hunt *et al.* 1978)

$$\left(\sum N + \frac{1}{2}\sum N'\right) - \left(\sum S + \frac{1}{2}\sum S'\right) = 0. \tag{3.1}$$

For case R1 there are two nodes located inside each SCV core, two half-saddles in the outer flow at the domain boundaries corresponding to the upwash and downwash regions and two half-saddles on the ridge surface, one at the ridge crest and the second at the bottom of the valley (figure 2*a*). Overall, the topology resembles typical flow topologies reported earlier for large-scale roughness-induced SCVs above rectangular ridges (Castro *et al.* 2021) and strip-type roughness (Stroh *et al.* 2016). It should be noted that the exact topology depends on the size of the SCVs and the ridge geometry, e.g. for rectangular ridges Castro *et al.* (2021) reported a total of 8 half-saddles on the ridge surface and channel wall.

With the emergence of net spanwise flow (case R3), instead of two half-saddles in the outer flow, a single saddle point appears in this region (figure 2*b*). This critical point is located above the SCV formed on the low-slope ridge side, where the top part of sidewash from this vortex (with $\bar{v} < 0$) is stagnated by the net spanwise flow (with $\bar{v} > 0$).

https://doi.org/10.1017/jfm.2024.634 Published online by Cambridge University Press

The number and location of half-saddles on the ridge surface remains unaffected. Increase in R, and consequent increase in the net spanwise flow magnitude, moves the saddle point in the wall-normal direction closer to the nodal point located inside the secondary current vortex formed on the low-slope ridge side (figure 2*c*). For case R∞, where the strongest net spanwise flow is observed, these two critical points (node and saddle) above the low-slope ridge side merge (figure 2*d*). The resultant flow topology in this region corresponds to the case of the merging of two critical points (Moffatt 2021).

For isosceles triangular ridges the nodal points that correspond to the centres of the secondary current vortices occur at an increasing distance from the wall as the ridge base width is increased (Zhdanov *et al.* 2024). This effect can also be observed for the present scalene triangles: with increasing R, the secondary current centre above the low-slope side moves further away from the wall whereas the corresponding nodal point above the high-slope side moves closer to the wall. As a result, the upper sidewash region of the high-slope ridge side SCV starts to become horizontally aligned with the lower sidewash region of the SCV above the low-slope ridge side, resulting in increasing net positive spanwise flow above the ridge crests as the slope imbalance increases. In addition, as the high-slope side SCV moves closer to the wall its lower sidewash region intensifies and starts to dominate the flow within the cavity, leading to net negative spanwise flow below the ridge crests, as discussed above for the mean spanwise velocity profiles (see figure 3*a*).

For cases R7 and R∞, an additional vortex, and consequently node, emerges between the ridge surface and the SCV formed over the high-slope ridge side, as can be clearly seen from the inset to figure 2(*d*), where mean flow streamlines are shown for this part of the domain. The flow topology in this region is very similar in both cases and for brevity is only shown for R∞. In addition, a saddle is formed between this vortex and the downwash part of the flow. The presence of this additional vortex shifts the location of the half-saddle point on the vertical ridge surface to a higher wall-normal location for case R∞, while for R7 this half-saddle remains at the bottom of the valley. In all cases, including those where nodes and saddles merge/appear, the number of critical points in the flow satisfies (3.1).

To summarise, highly asymmetric scalene ridges not only change the location of critical points, but fundamentally alter the topology of the secondary currents due merging of critical points and the emergence of new critical points. Above ridge crests the regions of SCVs with the same sign of $\bar{v}$ become horizontally aligned, giving rise to net spanwise flow. Alternatively, the observed flow topology for the scalene ridge cases could also be interpreted as the superposition of SCVs with a net spanwise flow. By subtracting the $\langle\bar{v}\rangle^+$ profiles from the corresponding $\bar{v}^+$ fields, the conventional topology of SCVs can be restored (see figure 4*b*).

3.3. *Decomposition of streamwise vorticity*

Further analysis of the observed secondary current patterns can be performed by applying the classification of Bradshaw (1987): SCVs and spanwise flow can be distinguished by the contributions of the spanwise and wall-normal velocity gradient terms to the streamwise vorticity of the mean flow $\bar{\Omega}_x = \partial\bar{w}/\partial y - \partial\bar{v}/\partial z$. Secondary current vortices are observed in the flow regions where $\partial\bar{v}/\partial z$ and $\partial\bar{w}/\partial y$ have similar magnitude, while spanwise flow occurs where $\partial\bar{v}/\partial z$ makes the dominant contribution to $\bar{\Omega}_x$. Contours of time- and phase-averaged streamwise vorticity contributions ($\partial\bar{v}/\partial z$, $\partial\bar{w}/\partial y$) for the present ridged surfaces are shown in figure 6. In all cases the two terms have similar magnitude close to and above the ridge crests, where SCVs are observed for these surfaces. These regions

https://doi.org/10.1017/jfm.2024.634 Published online by Cambridge University Press

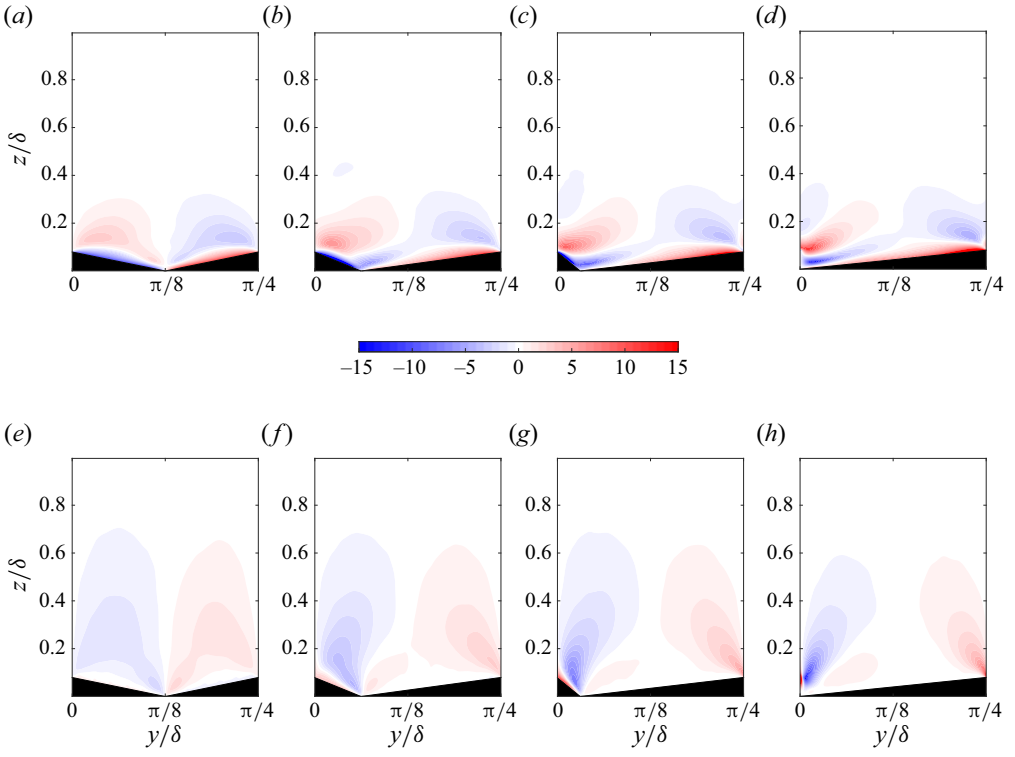


Figure 6. Contours of time- and phase-averaged streamwise vorticity components. (*a–d*) $\partial\overline{v}^{+}/\partial(z/\delta)$, (*e–h*) $\partial\overline{w}^{+}/\partial(y/\delta)$. (*a*,*e*) Case R1, (*b*,*f*) case R3, (*c*,*g*) case R7, (*d*,*h*) case R∞.

also correspond to the location of non-zero swirl strength (not shown), a quantity which is widely used to characterise SCVs.

Within the ridge canopy, the streamwise vorticity is formed predominantly by the $\partial\bar{v}/\partial z$ term, indicating the presence of spanwise flow, while the sign of $\partial\bar{v}/\partial z$ determines the direction of the local spanwise flow. In the case of ridges with equal side slopes (R1), spanwise flow regions are generated along both ridge sides from the centre of the cavity towards ridge crest (figure 6*a*). The magnitude of $\partial\bar{v}/\partial z$ closely matches over both sides, amounting to zero net spanwise flow. As the ridge cross-section symmetry is broken (cases R3, R7 and R∞), the spanwise flow still starts close to the midpoint between the two ridge crests in the y-direction. However, for scalene ridge cases this location does not correspond to the middle of the cavity as in the isosceles case, and the negative $\partial\bar{v}/\partial z$ region now extends over the low-slope side of the ridge, with the positive $\partial\bar{v}/\partial z$ contours not covering the whole low-slope side (figure 6*b–d*). As a result, regions of spanwise flow with different directions become imbalanced with stronger flow towards the high-slope ridge side, leading to the observed net spanwise flow within ridge canopy. The maximum difference in $\partial\bar{v}/\partial z$ magnitude increases as the ratio of ridge lateral slopes is changed from 3 to 7 followed by a drop as the ridge cross-section becomes right-angled triangle. This corresponds to the trends observed in the $\langle\bar{v}\rangle^{+}$ profiles in the region below the ridge crest (figure 3*a*).

As discussed in § 3.1, the magnitude of the net spanwise flow within the cavity attains the highest values for the R7 case, whereas the highest net spanwise flow above the ridged surfaces is observed for the right-angled ridge case R∞. Therefore, imbalance in $\partial\bar{v}/\partial z$

https://doi.org/10.1017/jfm.2024.634 Published online by Cambridge University Press

regions and hence the spanwise flow within the ridge canopy on its own cannot explain the increase in the net spanwise flow above the ridge crest. The effectiveness of the cavity shape in organising the flow within the cavity needs also to be taken into account. Cavity sides with gradual slopes (as for the present isosceles ridges and low-slope sides of scalene ridges) induce coherent flow parallel to them, which accelerates toward the ridge crest. As the ridge side slope increases (high-slope sides of scalene ridges) part of the spanwise flow is blocked by the ridge surface, with the maximum effect observed in the R∞ case, where the high-slope side is a vertical wall on which a stagnation point forms (see inset to figure 2*d*). This is also evident in the instantaneous velocity statistics, e.g. in the joint probability density function (j.p.d.f.) of the local spanwise and wall-normal velocity components $P(v, w)$ (see figure 7). Panels (*a–d*) show the joint p.d.f. for a point close to the high-slope side of the ridge and (*e–h*) for a point close to the low-slope side. The points are placed at a wall-normal location $z/\delta = 0.055$ and at a normal distance $d^+ = 4.2$ from the ridge surface. Near the left (high-slope) ridge side the j.p.d.f.s are dominated by $Q2$ and $Q4$ events, while close to the right (low-slope) side the dominant contributions come from $Q1$ and $Q3$ events. The shapes of the j.p.d.f.s reflect the changes in flow organisation within the cavity as ridge cross-sectional asymmetry is introduced. For the symmetric ridge case, the j.p.d.f.s for both near-ridge wall locations mirror each other with respect to $v^+ = 0$ and the most probable events are associated with negative v^+ close to the left ridge side and positive v^+ close to the right ridge side. As R is increased, the j.p.d.f.s for the high-slope ridge side show a clear change in their orientation with respect to the v^+ and w^+ axes with an increasing occurrence of high (positive and negative) w^+ events and a decrease in high v^+ events. For R∞ the shape of the j.p.d.f. becomes more aligned with the w^+-axis as more spanwise flow is deflected in the wall-normal direction by the vertical ridge side. In contrast, only very minor changes in the j.p.d.f.s are observed for the location close to the low-slope side of the ridge where the j.p.d.f.s consistently exhibit preferential alignment with the v^+-axis. Since secondary currents are uniquely determined by the distribution of the streamwise vorticity of the mean flow (Brundrett & Baines 1964; Nikitin, Popelenskaya & Stroh 2021), they can be analysed using the transport equation for $\bar{\Omega}_x$, which for a statistically stationary and streamwise homogeneous flow is given by

$$\bar{v}\frac{\partial \bar{\Omega}_x}{\partial y} + \bar{w}\frac{\partial \bar{\Omega}_x}{\partial z} - \nu\left(\frac{\partial^2 \bar{\Omega}_x}{\partial y^2} + \frac{\partial^2 \bar{\Omega}_x}{\partial z^2}\right) = S. \tag{3.2}$$

The first two terms on the left-hand side in (3.2) represent the advection of streamwise mean flow vorticity by the mean flow in the y–z plane, while the third term governs its diffusion by viscosity. The source term S on the right-hand side is responsible for production of $\bar{\Omega}_x$ and consists of spatial gradients of the in-plane Reynolds stresses

$$S = \underbrace{\frac{\partial^2 \overline{v'v'}}{\partial y \partial z} - \frac{\partial^2 \overline{w'w'}}{\partial y \partial z}}_{S_1} + \underbrace{\frac{\partial^2 \overline{v'w'}}{\partial z^2} - \frac{\partial^2 \overline{v'w'}}{\partial y^2}}_{S_2}. \tag{3.3}$$

The contours of the source term for the studied cases are presented in figure 8. As expected from previous studies (e.g. Castro & Kim 2024), the region of the highest vorticity production is located around the ridge crests, which represent a convex corner. For the symmetric ridge case, the regions of positive and negative S on the left and right ridge sides mirror each other – the source term has largely negative values over the left ridge side and positive values over the right side. As expected, S^+ changes its sign at the lines of symmetry (Nikitin *et al.* 2021), i.e. at the centre of the cavity and at the ridge crest.

https://doi.org/10.1017/jfm.2024.634 Published online by Cambridge University Press

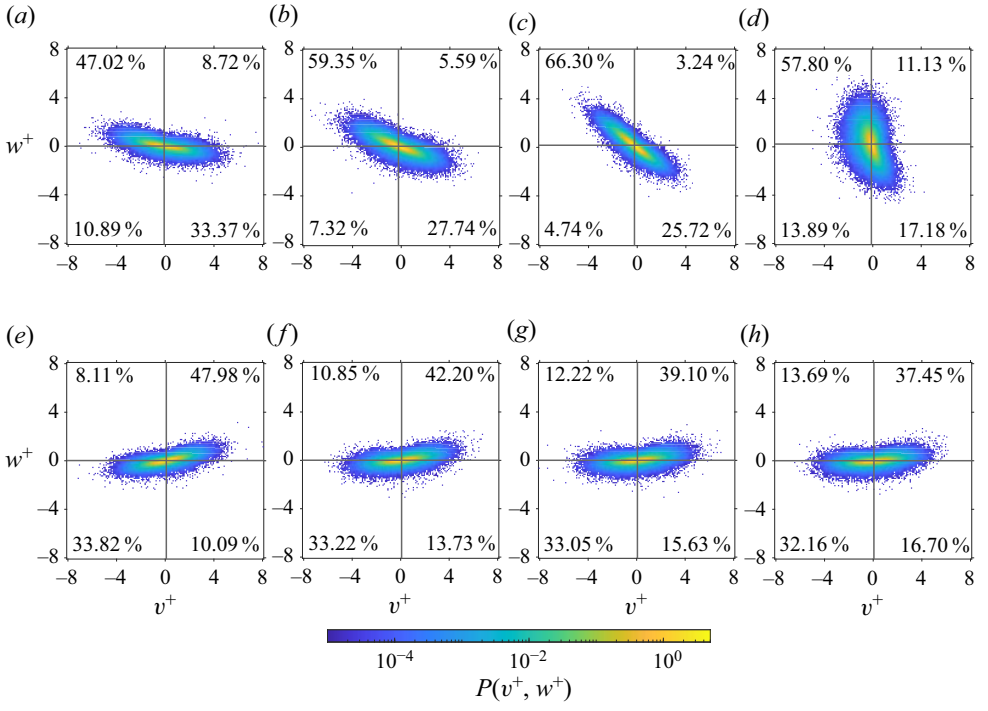


Figure 7. Joint probability density function of the spanwise (v^+) and wall-normal (w^+) velocity components at a wall-normal location $z/\delta = 0.055$ and normal distance $d^+ = 4.2$ from the ridge wall; (*a*,*e*) R1, (*b*,*f*) R3, (*c*,*g*) R7, (*d*,*h*) R∞. The top row (panels *a–d*) shows joint p.d.f.s close to the high-slope ridge side, bottom row (panels *e–h*) shows joint p.d.f.s close to the low-slope ridge side. The numbers in each panel show the probability of events in the corresponding quadrant.

For the scalene ridge cases, these lines of symmetry cease to exist. While the asymmetric ridge cases maintain largely positive values of S^+ over the low-slope side which increase in strength with R, the area of negative S^+ over the high-slope side shrinks in size and becomes squeezed by an area of positive S^+ originating at the ridge crest which tilts clockwise and intensifies as R increases. As a result, regions of positive S^+ become dominant above the ridge canopy.

This can also be observed from figure 9(*a*), where the spanwise profiles of the source term are shown for a distance of $\approx$30 wall units above the ridge crest. While for case R1 the S^+-profile is approximately point symmetric with respect to the centre of the cavity with a positive maximum over the right slope and a negative minimum over the left slope, the scalene cases show positive local maxima for both sides of the ridge and a negative minimum located close to the ridge crest location. The left maximum can be associated with the upper sidewash region of the SCV over the high-slope ridge side, the right maximum with the lower sidewash region of the SCV over the low-slope ridge side and the minimum with the strong upwash at the ridge crest, which is tilted towards the right for the asymmetric ridge cases.

To further explore the change of sign in S^+ over the high-slope ridge side, the spanwise profiles of S_1^+ and S_2^+ are considered, which for clarity are shown only for R1 and R∞ in figure 9(*b*). For case R1, S_1^+ and S_2^+ have similar values but opposite signs and thus production of $\bar{\Omega}_x$ is largely the result of slightly higher absolute values of S_2^+ compared

https://doi.org/10.1017/jfm.2024.634 Published online by Cambridge University Press

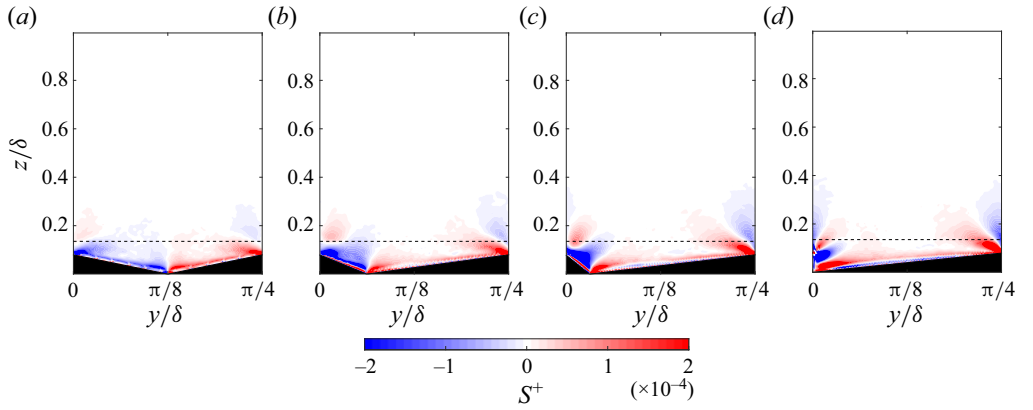


Figure 8. Contours of the source terms of the streamwise vorticity transport equation; (*a*) R1, (*b*) R3, (*c*) R7, (*d*) R∞. The thin horizontal dashed line in each panel marks the location for which profiles are plotted in figure 9.

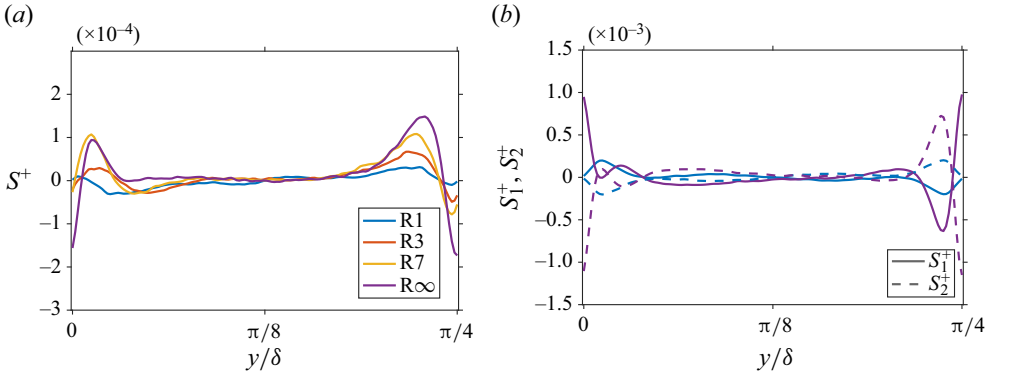


Figure 9. Spanwise profiles of (*a*) total source term S^+ in vorticity transport equation at $z^+ \approx 30$ above ridge crest for all cases, (*b*) two separate terms S_1^+ and S_2^+ for cases R1 and R∞.

with S_1^+. For case R∞, S_2^+ still dominates over S_1^+, but both S_1^+ and S_2^+ now take high absolute values at the ridge crest location. Over the high-slope ridge side around the maximum observed for S^+ in this case, S_1^+ develops a local minimum and S_2^+ changes its sign, developing a local maximum. Similar changes can be observed for the other scalene ridge cases.

3.4. *Spanwise pressure gradient and net spanwise flow (cross-flow)*

In three-dimensional turbulent boundary layers two primary types of spanwise/cross-flow are distinguished based on their origin: pressure driven (e.g. Coleman, Kim & Spalart 2000), i.e. due to imposed spanwise pressure gradient, and shear-driven (e.g. Abe 2020), i.e. due to spanwise wall movement. The former also corresponds to Prandtl's secondary currents of the first kind (Bradshaw 1987).

In the present DNS, ridged surfaces are treated as stationary no-slip walls and no mean spanwise pressure gradient is applied. While the ridge surfaces are stationary, the imbalance in the SCVs induced by the asymmetric ridges has, from a macroscopic perspective, a similar effect on the mean flow above the ridges as a wall that is slowly

https://doi.org/10.1017/jfm.2024.634 Published online by Cambridge University Press

moving in the positive y-direction (see schematic shown in figure 5*d*). Since the ridges on both channel walls mirror each other, the 'moving-wall effect' induced by the ridges is in the same direction for both the lower and the upper parts of the channel and thus no Couette-type profile is observed for the mean spanwise velocity component.

Within the scalene ridge canopies, the slope-induced imbalance of the flow over the ridge sides leads to the emergence of a mean spanwise pressure gradient, as can be observed from the double-averaged spanwise pressure gradient $\partial\langle\bar{p}\rangle/\partial y$ profiles (figure 5*b*). While for isosceles ridges the spanwise pressure gradient is close to zero across the whole channel, including the ridge canopy, for scalene ridge cases $\partial\langle\bar{p}\rangle/\partial y$ has largely non-zero values below the ridge crest. An increase in R leads to higher magnitude of $\partial\langle\bar{p}\rangle/\partial y$ in this region, which propagates further from the bottom of the valley towards the ridge crest, with high spanwise pressure gradient values observed across almost the entire ridge height in case R∞ (see inset in figure 5*b*). The resulting flow over the ridges causes a net transfer of spanwise momentum to the flow above the ridges through secondary current vortices and turbulent fluctuations, as can be observed from the corresponding profiles of the sum of in-plane Reynolds $\langle\overline{v'w'}\rangle^+$ and dispersive shear stress $\langle\tilde{v}\tilde{w}\rangle^+$ (figure 5*c*), giving rise to the observed net spanwise flow in the channel. The in-plane shear stresses vanish as z/δ approaches channel half-height as is expected for fully developed wall-shear-driven flow (Howard & Sandham 2000).

Since the flow above the ridges is not the direct result of a spanwise pressure gradient, the observed cross-flow cannot be classified as secondary current of Prandtl's first kind. Instead, as discussed in the previous sections, the observed net spanwise flow is caused by imbalanced and misaligned secondary currents of Prandtl's second kind. This unusual manifestation of secondary currents may therefore give rise to a new sub-division of secondary currents of the second kind – namely, those with vanishing net spanwise flow, i.e. the type widely reported in the literature for symmetric surfaces, and those where net spanwise flow emerges due to presence of symmetry-breaking effects.

4. Conclusions

Turbulent channel flow over scalene streamwise-aligned ridges has been investigated using DNS. The symmetry-breaking effects of a scalene ridge geometry are evident in the mean flow, where net spanwise flow emerges. The present results show that net spanwise flow can be produced by streamwise homogeneous surfaces due to their geometry, in contrast to previous studies on three-dimensional turbulent boundary layers where cross-flow was introduced by surface shear (moving wall), or the presence of a spanwise pressure gradient, e.g. due to duct curvature or over a swept wing. The magnitude of spanwise flow is directly influenced by the ridge cross-sectional asymmetry, with the maximum $\langle\bar{v}\rangle^+$ above the ridge crests induced by the right-angled triangular ridges. Although the spanwise flow is weak compared with the streamwise flow, it has a significant impact on the overall mean flow topology, altering the number and location of critical points compared with the conventional topology of SCVs generated by symmetric ridges or strip-type roughness. The observed net spanwise flow in the scalene ridge cases can be attributed to the increasing alignment between the upper sidewash region of the high-slope SCV with the lower sidewash region of the SCV over the low-slope side as the centre of the high-slope SCV moves closer to the wall and the centre of the SCV over the low-slope side moves further away from the wall with increasing imbalance in the ridge slopes.

The investigated surfaces with asymmetric ridges may have applications for flow control, mixing and drag reduction. It should be noted that scalene triangular cross-section

https://doi.org/10.1017/jfm.2024.634 Published online by Cambridge University Press

has also been investigated in the context of riblets (Modesti *et al.* 2021), which, similarly to ridges, generate SCVs, although of a much smaller size. For right-angled triangular riblets, Modesti *et al.* (2021) reported the presence of spanwise flow regions above and below riblet crests in the same direction as observed for scalene ridges in the present study. However, due to the minimal-channel approach used by Modesti *et al.* (2021) it is not clear whether net spanwise flow extends to the outer layer of the flow as in the present study. For equilateral ridges, the strength of secondary currents intensifies with an increase in Reynolds number (Zhdanov *et al.* 2024), therefore, it would be of interest to determine whether the net spanwise flow is sensitive to this parameter. Finally, it remains to be tested whether the magnitude of the spanwise flow can be increased by optimisation of the surface geometry, e.g. by varying the spanwise effective slope.

Acknowledgements. This work used the ARCHER2 UK National Supercomputing Service (https://www.archer2.ac.uk).

Funding. We gratefully acknowledge support for this work by the United Kingdom's Engineering and Physical Sciences Research Council under grant number EP/V002066/1.

Declaration of interests. The authors report no conflict of interest.

Data availability statement. The data that support the findings of this study are openly available in the University of Glasgow Enlighten repository at http://doi.org/10.5525/gla.researchdata.1680.

Author ORCIDs.
Oleksandr Zhdanov https://orcid.org/0000-0002-1742-9765;
Angela Busse https://orcid.org/0000-0002-3496-6036.

References

Abe, H. 2020 Direct numerical simulation of a non-equilibrium three-dimensional turbulent boundary layer over a flat plate. *J. Fluid Mech.* **902**, A20.

Bradshaw, P. 1987 Turbulent secondary flows. *Annu. Rev. Fluid Mech.* **19** (1), 53–74.

Brundrett, E. & Baines, W.D. 1964 The production and diffusion of vorticity in duct flow. *J. Fluid Mech.* **19** (3), 375–394.

Busse, A., Lützner, M. & Sandham, N.D. 2015 Direct numerical simulation of turbulent flow over a rough surface based on a surface scan. *Comput. Fluids* **116**, 129–147.

Busse, A. & Zhdanov, O. 2022 Direct numerical simulations of turbulent channel flow over ratchet roughness. *Flow Turbul. Combust.* **109** (4), 1195–1213.

Castro, I.P. & Kim, J.W. 2024 Secondary motions in turbulent ribbed channel flows. *J. Fluid Mech.* **988**, A2.

Castro, I.P., Kim, J.W., Stroh, A. & Lim, H.C. 2021 Channel flow with large longitudinal ribs. *J. Fluid Mech.* **915**, A92.

Coleman, G.N., Kim, J. & Spalart, P.R. 2000 A numerical study of strained three-dimensional wall-bounded turbulence. *J. Fluid Mech.* **416**, 75–116.

Gray, W.G. & Lee, P.C.Y. 1977 On the theorems for local volume averaging of multiphase systems. *Intl J. Multiphase Flow* **3** (4), 333–340.

Hinze, J.O. 1967 Secondary currents in wall turbulence. *Phys. Fluids* **10** (9), S122–S125.

Howard, R.J.A. & Sandham, N.D. 2000 Simulation and modelling of a skewed turbulent channel flow. *Flow Turbul. Combust.* **65**, 83–109.

Hunt, J.C.R., Abell, C.J., Peterka, J.A. & Woo, H. 1978 Kinematical studies of the flows around free or surface-mounted obstacles; applying topology to flow visualization. *J. Fluid Mech.* **86** (1), 179–200.

Hwang, H.G. & Lee, J.H. 2018 Secondary flows in turbulent boundary layers over longitudinal surface roughness. *Phys. Rev. Fluids* **3** (1), 014608.

Jelly, T.O., Ramani, A., Nugroho, B., Hutchins, N. & Busse, A. 2022 Impact of spanwise effective slope upon rough-wall turbulent channel flow. *J. Fluid Mech.* **951**, A1.

Lee, M. & Moser, R.D. 2015 Direct numerical simulation of turbulent channel flow up to $Re_\tau \approx 5200$. *J. Fluid Mech.* **774**, 395–415.

https://doi.org/10.1017/jfm.2024.634 Published online by Cambridge University Press

MEDJNOUN, T., VANDERWEL, C. & GANAPATHISUBRAMANI, B. 2020 Effects of heterogeneous surface geometry on secondary flows in turbulent boundary layers. *J. Fluid Mech.* **886**, A31.

MODESTI, D., ENDRIKAT, S., HUTCHINS, N. & CHUNG, D. 2021 Dispersive stresses in turbulent flow over riblets. *J. Fluid Mech.* **917**, A55.

MOFFATT, H.K. 2021 Some topological aspects of fluid dynamics. *J. Fluid Mech.* **914**, P1.

NAPOLI, E., ARMENIO, V. & DE MARCHIS, M. 2008 The effect of the slope of irregularly distributed roughness elements on turbulent wall-bounded flows. *J. Fluid Mech.* **613**, 385–394.

NIKITIN, N.V., POPELENSKAYA, N.V. & STROH, A. 2021 Prandtl's secondary flows of the second kind, problems of description, prediction, and simulation. *Fluid Dyn.* **56** (4), 513–538.

NIKORA, V., MCEWAN, I., MCLEAN, S., COLEMAN, S., POKRAJAC, D. & WALTERS, R. 2007 Double-averaging concept for rough-bed open-channel and overland flows: theoretical background. *J. Hydraul. Engng* **133** (8), 873–883.

PRANDTL, L. 1952 *Essentials of Fluid Dynamics: with Applications to Hydraulics, Aeronautics, Meteorology, and Other Subjects*. Blackie.

RAUPACH, M.R. & SHAW, R.H. 1982 Averaging procedures for flow within vegetation canopies. *Boundary-Layer Meteorol.* **22** (1), 79–90.

STROH, A., HASEGAWA, Y., KRIEGSEIS, J. & FROHNAPFEL, B. 2016 Secondary vortices over surfaces with spanwise varying drag. *J. Turbul.* **17** (12), 1142–1158.

STROH, A., SCHÄFER, K., FOROOGHI, P. & FROHNAPFEL, B. 2020 Secondary flow and heat transfer in turbulent flow over streamwise ridges. *Intl J. Heat Fluid Flow* **81**, 108518.

VANDERWEL, C. & GANAPATHISUBRAMANI, B. 2015 Effects of spanwise spacing on large-scale secondary flows in rough-wall turbulent boundary layers. *J. Fluid Mech.* **774**, R2.

WANG, Z.-Q. & CHENG, N.-S. 2006 Time-mean structure of secondary flows in open channel with longitudinal bedforms. *Adv. Water Resour.* **29** (11), 1634–1649.

YANG, J. & BALARAS, E. 2006 An embedded-boundary formulation for large-eddy simulation of turbulent flows interacting with moving boundaries. *J. Comput. Phys.* **215** (1), 12–40.

ZAMPIRON, A., CAMERON, S. & NIKORA, V. 2020 Secondary currents and very-large-scale motions in open-channel flow over streamwise ridges. *J. Fluid Mech.* **887**, A17.

ZHDANOV, O., JELLY, T.O. & BUSSE, A. 2024 Influence of ridge spacing, ridge width, and Reynolds number on secondary currents in turbulent channel flow over triangular ridges. *Flow Turbul. Combust.* **112**, 105–128.

https://doi.org/10.1017/jfm.2024.634 Published online by Cambridge University Press